Lagrangian Measurements of Waves and Turbulence in Stratified Flows

ERIC A. D'ASARO

Applied Physics Laboratory and School of Oceanography, University of Washington, Seattle, Washington

REN-CHIEH LIEN

Applied Physics Laboratory, University of Washington, Seattle, Washington

ABSTRACT

Stratified flows are often a mixture of waves and turbulence. Here, Lagrangian frequency is used to distinguish these two types of motion.

A set of 52 Lagrangian float trajectories from Knight Inlet and 10 trajectories from below the mixed layer in the wintertime northeast Pacific were analyzed using frequency spectra. A subset of 28 trajectories transit the Knight Inlet sill where energetic internal waves and strong turbulent mixing coexist.

Vertical velocity spectra show a progression from a nearly Garrett–Munk internal wave spectrum at low energies to a shape characteristic of homogeneous turbulence at high energies. All spectra show a break in slope at a frequency close to the buoyancy frequency N. Spectra from the Knight Inlet sill are analyzed in more detail. For "subbuoyant" frequencies (less than N) all 28 spectra exhibit a ratio of vertical-to-horizontal kinetic energy that varies with frequency as predicted by the linear internal wave equations. All spectra have a shape similar to that of the Garrett–Munk internal wave spectrum at subbuoyant frequencies. These motions are much more like waves than turbulence. For "superbuoyant" frequencies (greater than N) all 28 spectra are isotropic and exhibit the -2 spectral slope of inertial subrange homogeneous turbulence. These motions appear to be turbulent.

These data suggest that stratified flows may be modeled as the sum of nearly isotropic turbulence with superbuoyant Lagrangian frequencies and anisotropic internal waves with subbuoyant Lagrangian frequencies. The horizontal velocities are larger than the vertical velocities for the internal wave component but approximately equal for the turbulent component. Vertical kinetic energy is therefore a better indicator of turbulent kinetic energy than is horizontal or total kinetic energy.

1. Introduction

Nearly 30 years ago R. W. Stewart (Stewart 1969) wrote about the study of stably stratified turbulence: "[It] is greatly complicated by the fact that we have two quite different types of flows intermingled: turbulence and internal gravity waves. Also, the inferences that we should like to draw for the unmeasured aspects of the field are totally different for the two kinds of motion. And there is the further complication of a nonlinear coupling that causes energy to flow between them. . . . Two questions must then be asked: first, Is it *desirable* to be able to distinguish between turbulence and waves; and second, Is it *possible*? To the first question, I would reply that it clearly *is* desirable to attempt to make this distinction. It is never possible to measure all the features of the particular field. One must measure some aspects and infer the rest. The inferences which would be drawn from a measurement of some aspects of a wave field should be quite different from the inferences drawn from similar measurements in turbulent field."

There is, of course, no exact division between waves and turbulence. For example, an internal wave packet constructed from purely linear waves propagating in a sheared background can become highly nonlinear and develop regions of strong turbulence (Winters and D'Asaro 1994; Lin et al. 1995). This "breaking wave" is neither "wave" nor "turbulence" but contains aspects of both.

Similarly, "stratified turbulence" can be generated by energetic mixing of a stratified fluid in a laboratory tank (Stillinger et al. 1983; Itsweire et al. 1986) or simulated by initializing a numerical model of a stratified fluid with an initial state characteristic of unstratified turbulence (Gertz and Yamazaki 1993; Holt et al. 1992). The initial condition will, in general, project onto the

Corresponding author address: E. A. D'Asaro, Applied Physics Laboratory, University of Washington, 1013 N.E. 40th St., Seattle, WA 98105.
E-mail: dasaro@apl.washington.edu

linear wave modes of the stratified fluid. Hanazaki and Hunt (1996) compute the subsequent evolution of these modes and find the ''behavior of stably stratified turbulence in . . . [these experiments] . . . can largely be explained by linear oscillations and molecular or eddy diffusion rather than by any new kinds of nonlinear mixing processes.'' Thus, stratified flows set up to be ''turbulent'' can sometimes contain large ''wave'' components that dominate many aspects of their evolution.

Nevertheless, one can make several distinctions between wave-dominated flows and turbulence-dominated flows. Waves obey a dispersion relation. They are thus narrowband in the sense that they have significant energy only in a very small volume of wavenumber–frequency space. Internal gravity waves in a fluid of constant buoyancy frequency N and inertial frequency f only have energy along the curves

$$\omega^2 - f^2 = \frac{(N^2 - f^2)(k^2 + l^2)}{k^2 + l^2 + m^2}, \qquad (1)$$

where ω is the frequency, k and l are the horizontal wavenumbers, and m is the vertical wavenumber. In contrast, unstratified turbulent flows are broadband and occupy a continuum in frequency–wavenumber space. Lien et al. (1998) show a plausible spectrum. Only a general relationship exists between time and space scales; a flow with spatial scale L_t and kinetic energy Q^2 will have a typical time T_t of about L_t/Q.

Waves have exact relationships between the fluctuations in each velocity component and in the stratification. For a single sinusoidal internal gravity wave the velocity fluctuations describe an ellipse whose major axis is in the same direction as the group velocity and whose plane is perpendicular to the wavenumber vector. The plane defined by the group velocity and wavenumber vector is vertical (Phillips 1977). The relative magnitudes of the velocity components are a function only of frequency,

$$\frac{\Phi_u + \Phi_v + \Phi_w}{\Phi_w} = \frac{N^2(\omega^2 + f^2) - 2\omega^2 f^2}{\omega^2(\omega^2 - f^2)} \approx \frac{N^2}{\omega^2}, \quad (2)$$

where Φ_u, Φ_v, and Φ_w are spectra of the horizontal (u, v) and vertical velocity (w) components. The approximation applies for $\omega \gg f$. For $\omega \ll N$, (1) and (2) indicate that the waves are highly anisotropic; the vertical kinetic energy is much smaller than the horizontal kinetic energy and the vertical wavenumber is much larger than the horizontal wavenumber. Note that (2) applies not only to a single sinusoidal wave but to the average of the sum of randomly phased waves with frequency ω. In contrast, unstratified turbulence is usually close to isotropic, except in environments with strong anisotropic forcing. Accordingly, the vertical and horizontal kinetic energies are nearly equal, as are the characteristic vertical and horizontal wavenumbers.

Waves remember their initial conditions for many wave periods. In a purely linear system with normal modes, no energy is exchanged between the modes, and each retains its initial amplitude and phase. Real fluid flows always have some nonlinearity and thus exchange energy between modes. The spectrum of oceanic internal waves, for example, tends to assume a universal shape described by the Garrett–Munk (GM) spectrum. The time required for this spectrum to emerge from an arbitrary initial condition is not well known, but it is certainly many wave periods (Müller et al. 1986; Winters and D'Asaro 1997). In contrast, most high-Reynolds-number turbulent flows develop an inertial subrange spectrum ($-5/3$ wavenumber spectral slope) within a time of approximately T_t.

Finally, waves mix weakly whereas turbulence mixes strongly. Waves, being only weakly nonlinear, only slightly distort the background density surfaces. They therefore only slightly enhance the rates of molecular diffusion. In contrast, high-Reynolds-number turbulent flows greatly distort density surfaces, resulting in greatly enhanced diffusion. This is perhaps the most important distinction between waves and turbulence and the end point for Stewart's (1969) discussion.

In this paper, we attempt to distinguish between waves and turbulence by examining their Lagrangian properties. The key measurements are trajectories of neutrally buoyant *Lagrangian floats* [section 3b(1)], which accurately follow the three-dimensional motion of water parcels. In unstratified turbulent flows these floats exhibit an inertial subrange spectrum in Lagrangian frequency consistent with Kolmogorov theory (section 2a) (Lien et al. 1998). We use the presence of this spectrum, plus isotropy, as an indicator of turbulent flow. In an internal wave field, the floats measure the wave frequency relative to the local water velocity, that is, the *intrinsic* frequency. In a sheared flow, expressions (1) and (2) apply if ω is the intrinsic frequency and if the WKB approximation is valid. We therefore use (2), and a GM-like spectrum (section 2b), as an indicator of internal waves.

We apply these criteria (section 5) first to an upper-ocean thermocline, where there is little turbulence, and then to data both close to and away from the sill of Knight Inlet, British Columbia. The sill region is a high-energy environment with a mixture of waves and turbulence (section 4). The main result is that motions with a Lagrangian frequency less than N (subbuoyant) are consistent with internal waves in both environments, whereas those with a Lagrangian frequency greater than N (superbuoyant) are consistent with turbulence only in the high-energy environment. The anisotropy of the flow is due to the internal wave component. The main conclusion, discussed in section 7, is that waves can be separated from turbulence by using the Lagrangian frequency. Implications for the parameterization of mixing in stratified fluids are discussed in a second paper (D'Asaro and Lien 2000).
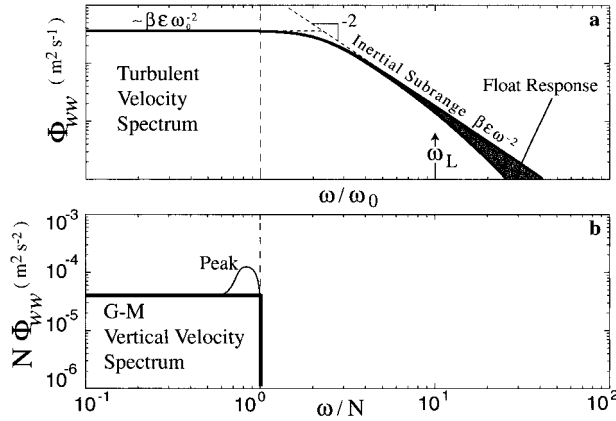
FIG. 1. Model spectra of velocity in (a) homogeneous isotropic turbulence and (b) a Garrett–Munk (GM) internal wave field with an intermittant peak near N. Vertical dashed line indicates the large-eddy frequency ω_0 in (a) and N in (b). Shaded region in (a) shows the correction due to a finite-sized float for $\omega_L/\omega_0 = 10$.

2. Lagrangian velocity spectra of waves and turbulence

a. Homogeneous turbulence

Lien et al. (1998) describe and model Lagrangian velocity spectra measured in unstratified, high-Reynolds-number oceanic turbulence. The observed spectra can be described by two parameters: the large-eddy frequency ω_0 and the rate of kinetic energy dissipation ε. Measurement of these spectra by a float of size L adds a third parameter, the float-size frequency $\omega_L = (\varepsilon/L^2)^{1/3}$. In homogeneous turbulence, ω_0 is determined by the outer parameters of the flow. Thus in a boundary layer of depth H, $\omega_0 \approx w^*/H$, where w^* is a typical vertical velocity.

Figure 1a shows the form of the spectrum. An *inertial subrange* of form $\beta\varepsilon\omega^{-2}$ exists for frequencies larger than about $3\omega_0$ and smaller than the Kolmogorov frequency $\omega_K = (\varepsilon/\nu)^{1/2}$, where ν is the viscosity (Corrsin 1957). The Kolmogorov constant β is 1–2 (Lien et al. 1998); $\beta = 1.8$ is used in this paper. Spectra measured by floats are attenuated for frequencies of about ω_L and larger, as shown by the shaded region in Fig. 1a. For frequencies below ω_0 the vertical velocity spectrum is approximately white.

Lien et al. (1998) compute the Lagrangian spectrum for isotropic, homogeneous turbulence, following the theory described by Fung et al. (1992). The vertical velocity spectrum (m² s⁻¹) is

$$\Phi_w^0(\omega) = \frac{\beta\varepsilon}{\omega^2} B\left(\frac{\omega}{\omega_0}\right), \tag{3}$$

where B sets the shape of the spectrum. In the inertial subrange, $B = 1$. The spectrum measured by a float is

$$\Phi_w^F(\omega) = \frac{\beta\varepsilon}{\omega^2} B\left(\frac{\omega}{\omega_0}\right) G\left(\frac{\omega}{\omega_L}\right), \tag{4}$$

where G is a response function that quantifies the attenuation of the spectrum at high frequencies due to the finite size of the float. For $\omega \ll \omega_L$, $G = 1$. Lien et al. (1998) compute exact forms numerically and find the following empirical fits:

$$B\left(\frac{\omega}{\omega_0}\right) = \left[1 + \left(2.2\frac{\omega_0}{\omega}\right)^4\right]^{-0.5} \tag{5}$$

$$G\left(\frac{\omega}{\omega_L}\right) = \left[1 + \left(0.63\frac{\omega}{\omega_L}\right)^2\right]^{-0.8}. \tag{6}$$

Note that B becomes proportional to $(\omega/\omega_0)^2$ for $\omega^2 \ll \omega_0^2$ so that Φ_w becomes white; G becomes proportional to $(\omega/\omega_L)^{-1.6}$ for $\omega^2 \gg \omega_L^2$ so that Φ_w has a spectral slope of almost -4. The effect of the finite float size can be partially removed from measured spectra by fitting (4) to the observed spectra, estimating ε, and computing

$$\Phi_w^0(\omega) = \frac{\Phi_w^F(\omega)}{G\left(\dfrac{\omega}{\omega_L}\right)}. \tag{7}$$

This spectral form has the undesirable property that displacement $\xi = \int w \, dt$ has infinite variance due to its -2 spectral slope at low frequencies. This is appropriate for homogeneous turbulence in an unbounded domain and appears to fit our boundary layer data well. However, the spectrum must necessarily have a flatter slope at low frequencies in any system where the particle displacements are bounded.

b. Garrett–Munk internal waves

Velocity spectra made most places in the ocean show a nearly universal form in the internal wave frequency band $f < \omega < N$. This implies that the wave spectrum relaxes toward this form regardless of initial conditions or forcing. Nonlinear wave–wave interactions (Müller et al. 1986) are generally thought to be responsible for the relaxation. This GM form (Garrett and Munk 1975) obeys the WKB scaling laws for internal waves; spectra of vertical velocity are proportional to N^{-1}, while spectra of horizontal velocity are proportional to N. We use a GM form for vertical velocity, which is white (Fig. 1b) for $\omega \leq N$ and drops to zero for $\omega > N$. The corresponding GM form for horizontal velocity (not shown) has a slope of -2, consistent with the vertical velocity spectra and Eq. (2).

Real oceanic spectra generally follow the GM form least well near N and f. None of our data are sufficiently long to resolve f. Both in our data and in the historical data a peak is often, but not always, present near N, as shown schematically in Fig. 1b. In the open ocean thermocline, this is thought to arise from the failure of the WKB approximation (Desaubies 1975). In coastal regions it has also been attributed to the presence of in-

ternal solitary waves (F. Henyey 1998, personal communication).

The GM frequency spectrum is an Eulerian frequency spectrum, tuned to match observations from moored current meters. In this paper we compare it to Lagrangian frequency spectra from floats. The GM wavenumber spectrum is red at each frequency, so the energy at each frequency is mostly due to the low internal wave modes. Since these have large phase speeds compared to their typical velocities, Doppler shifting should be relatively small, and we expect little difference between the Eulerian and Langrangian frequency spectra. This argument is supported by our limited observations from the open ocean [section 5d(1)] in which Lagrangian frequency spectra are very similar to the expected Eulerian GM spectrum.

c. Wave-driven turbulence

Most of the turbulence in the ocean interior is probably due to internal wave breaking. In this case the two spectra in Fig. 1 must be related. One way to do this is to, first, set $\omega_0 \approx N$ and, second, match the two spectral levels at $\omega \approx N$.

The first assumption, $\omega_0 \approx N$, is *Ozmidov scaling*. Usually, this is expressed by stating that the spatial scales of turbulence are limited by stratification so that the upper limit of the inertial subrange is set by N. In this case the largest eddies in the inertial subrange have the Ozmidov scale $L_O = \varepsilon^{1/2} N^{-3/2}$ (Ozmidov 1965). Here, we make the equivalent statement that the largest eddies in the inertial subrange have a frequency N.

The second assumption, matching the turbulence and GM spectral levels, Figs. 1a and 1b at $\omega \approx N$, is not generally true since turbulence levels in the ocean are usually very small. A major result of this paper is to show that it can be true in regions of high turbulence. D'Asaro and Lien (2000) explore the implications of this assumption for the physics and parameterization of mixing in stratified fluids.

3. Measurements

a. Knight Inlet

Most of the measurements described here were made in a fjord, Knight Inlet in British Columbia. The inlet is about 100 km long, averages 3 km wide, and is strongly stratified by freshwater from the Klinaklini River during the summer months. The circulation and stratification are strongly influenced by a narrow (1 km) and shallow (60 m) sill in the otherwise deep (400 m) fjord. Generally weak (0.1 m s^{-1}) barotropic tidal currents are accelerated to greater than 1 m s^{-1} over the sill, leading to a rich mix of internal waves, stratified turbulence, and hydraulically controlled flow. This has made Knight Inlet the focus of a large number of studies of fjord circulation (Farmer and Freeland 1983; Stacey and Pond
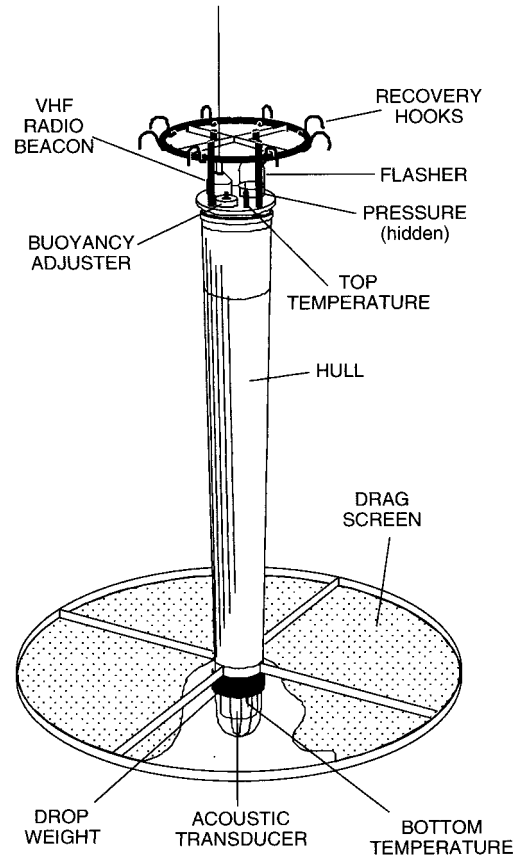

FIG. 2. A Lagrangian float (MLF).

1997), solitary waves and bores (Farmer and Smith 1980), and stratified turbulence (Gargett et al. 1984).

Measurements were made as part of a multiinvestigator study of internal waves and sill flows in Knight Inlet in August and September 1995. Much of the work consisted of detailed studies of the circulation (Klymak and Gregg 1999, manuscript submitted to *J. Geophys. Res.*), internal waves and bores, and mixing processes (Farmer and Armi 1999a,b). In this paper, however, we ignore these details, treat the flow in the vicinity of the sill as a mixture of waves and turbulence (section 4), and attempt to separate the two types of motions.

b. Knight Inlet instrumentation

1) LAGRANGIAN FLOATS

(i) Basic design

Measurements of 3D Lagrangian trajectories were taken using mixed layer Lagrangian floats (MLFs) designed to track the three-dimensional motion of water parcels. Each MLF consists of a 1.5-m-long cylindrical hull and a 1.2-m-diameter perforated drag screen (Fig. 2). The float's compressibility matches closely that of seawater, so it remains neutrally buoyant through large vertical excursions. The float measures its depth from

pressure and its vertical velocity from the derivative of pressure with time. Temperature is measured at both ends of the float. In Knight Inlet, however, density is controlled by salinity and cannot be reliably estimated from temperature measurements. Details of the instrumentation are described by D'Asaro et al. (1996), henceforth DFOD.

(ii) Acoustic tracking

The horizontal position and velocity of each MLF were determined by acoustic tracking. Acoustic pulses were transmitted from surface buoys loosely moored on the sill or left free to drift near the floats. The positions of the buoys were tracked to an accuracy of a few meters using GPS. Data were reprocessed with GPSPACE (available from Geodetic Survey Division, Natural Resources Division of the Canadian Government: www.geod.nrcan.gc.ca). This reduces errors due to "selective availability" and ionospheric noise by applying GPS clock drift and ephemeris corrections estimated from a worldwide set of fixed GPS receivers. The transmission time of each pulse was determined with an accuracy of a few microseconds using the time base in the GPS receivers.

Most floats were tracked by three or four surface buoys; a few had only two. Each buoy transmitted a pulse every 40 s. The transmisions were offset so that a different buoy transmitted every 10 s. Tracking ranges of up to 8 km were achieved at times.

Two schemes were used to obtain positions. For most trajectories the "low accuracy" scheme was used. The arrival time of each pulse at each MLF was recorded by the MLF to an accuracy of 3.5 ms, subject to an unknown clock offset and drift. The arrival times were linearly interpolated onto a uniform 36-s grid along with the depth of the float and the positions of the surface buoys. An initial guess of the float tracks was estimated by triangulation from the various pairs of buoys. The final tracks were obtained by varying the float positions, clock drift, clock offset, and average speed of sound in order to minimize the deviation of the predicted arrival times from those measured. Clock drift, offset, and sound speed were held constant for each float trajectory in the minimization. The quality of the fits was monitored by comparing the computed and measured speed of sound and the accuracy with which the float deployment and recovery positions were predicted. Spurious acoustic pulses were edited manually. A few float trajectories were tracked by only two buoys; clock drift and offset for these were estimated from the launch and recovery positions and the drift rates for other trajectories. The final tracks had an rms difference of 30–60 m between the observed and calculated ranges from the buoys to the floats, depending on the geometry and number of sources. Spectra of horizontal velocity were consistent with a tracking noise of about 30 m rms. This is roughly consistent with the bit error, 5 m, multiplied

by the estimated error amplification in the tracking, about a factor of 5. Absolute position uncertainty is certainly more than this, but the errors probably vary only slowly with range and will thus have little effect on the computed horizontal velocity.

Some float trajectories were calculated with the "high accuracy" scheme. Each MLF transmitted an acoustic pulse at a fixed time after receiving a pulse from one of the surface buoys. The arrival times of acoustic pulses from the floats were recorded at each buoy with high accuracy, as were the arrival times of pulses transmitted from the other buoys. With four buoys, there were 44 different acoustic paths; with three buoys there were 24 paths. A very large number of additional pulse arrivals were due to bottom reflection and multipathing. The direct paths were extracted from these using the "low accuracy" float tracks as a guide, and the arrival times were interpolated onto a 36 s grid. The acoustic travel time between buoys provided a consistency check on the GPS tracking and assumed sound speed. The data were consistent, once outliers were removed, to a few meters in range or, equivalently, about 1 m s^{-1} in sound speed. The many different paths traveling between the buoys and floats greatly overdetermined the physical ranges from the floats to the buoys and allowed spurious pulse arrival times to be edited. The resulting float-to-buoy ranges were consistent with the many pulse arrival times to an accuracy of a few meters. Tracks were extracted from these using a least squares fit.

Acoustic tracking noise appears in each horizontal velocity spectrum as a change from an approximately -2 slope to an approximately $+2$ slope. Since the noise level changes somewhat for different trajectories, each spectrum was truncated at either the end of the region with a -2 slope or at the point where it fell below the spectrum owing to an rms error of 30 m for the "low resolution" tracking and 5 m for the "high resolution" tracking.

(iii) Errors

The MLF is imperfectly Lagrangian, for several reasons. First, it is much larger than the Kolmogorov scale and can therefore, at best, follow the average motion of the surrounding water, rather than the motion of an individual molecule (see section 2a). Second, the float's density may differ from that of the surrounding water; it will then rise or fall relative to the water. Knight Inlet is highly stratified, so the floats settled to the level where their density matched that of the water. We accelerated this process by using a pressure-activated drop weight, set to release at approximately the correct isopycnal. The vertical velocity of the float relative to the water due to any residual density difference was reduced to a few millimeters per second by the large drag screen (see DFOD). Third, the float is asymmetrical. The hydrodynamic force on the float is not directly opposed to the relative velocity of the water, so the float can move

in unexpected directions in the presence of strong shear. Although we have observed this behavior using scale-model floats in the laboratory, we have seen no evidence of it in field data. Finally, since the float's sensors are offset from its center, they do not follow a Lagrangian trajectory even if its center does.

The MLFs have been deployed in a variety of environments. DFOD, D'Asaro and Dairiki (1997), and Lien et al. (1998) describe measurements in surface and internal wave fields, in turbulent mixed layers, and in turbulent tidal channels. Overall, the floats appear to be accurately Lagrangian as long as the water velocities are sufficiently large in magnitude and spatial scale.

2) OTHER MEASUREMENTS

In Knight Inlet, measurements were made from three vessels, each carrying a CTD unit, an Acoustic Doppler Current Profiler (ADCP), and an echosounder. The CSS *Vector* carried a 300-kHz RD Instruments broadband ADCP and a Guildline CTD. The R/V *Miller* carried a 150-kHz RDI broadband ADCP and a Seabird 9/11 CTD unit mounted in a towed sled to enable underway profiling at speeds of 3 m s^{-1}. The CRV *Bazan Bay* carried a 300-kHz RDI narrowband ADCP and a Seabird 19 Seacat CTD unit. All three vessels carried Biosonics 120-kHz echosounders. All were tracked by GPS; these data were postprocessed using GPSPACE [see section 3c(1ii)] to obtain accuracies of a few meters every few seconds.

In this paper, these data are used only to determine the stratification and shear associated with the Lagrangian float trajectories. The complete trajectories were subjectively divided into segments representing different flow regimes (see section 5b). CTD casts within 500 m and 1 h of each float track were averaged to produce an N profile for that segment. These were averaged over the depth range of the float to compute a typical N value for that segment. The available CTD data did not produce a reliable N for most trajectories. Sometimes no casts were available. Often only a few were available; these were often biased toward the centerline of the channel. The final N value for each segment therefore has a large uncertainty due to poor sampling of variations in N along that trajectory. This is quantified in section 5c.

c. Ocean thermocline

For comparison, we include some float data from the northeast Pacific taken in February 1993 and 1995 as part of studies of mixed layer turbulence. The floats and tracking system were identical to those used in Knight Inlet. A variant of the "high accuracy" float-tracking scheme was used. CTD data accompanying each float deployment were from a high-quality SeaBird 9/11 with dual sensors. We use data from floats intentionally or unintentionally ballasted to depths below the mixed lay-
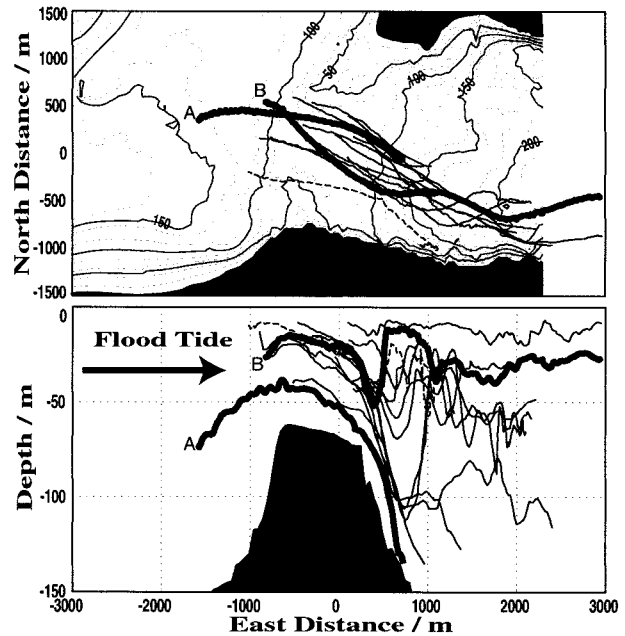

FIG. 3. Trajectories of all floats that traveled over the sill on strong flood tides. (a) Plan and (b) side views are shown. Two trajectories are highlighted for clarity. The ocean is to the left.

er, some in the entrainment zone just below the mixed layer (50–80 m) and one in the permanent pycnocline around 125-m depth. These are wave-dominated environments; there is no evidence of strong turbulence in the float or CTD records.

4. Flow regime

Figure 3 shows the trajectories of all floats that traveled over the sill during strong flood tides. The floats were deployed on different days, at different phases of the flood tide, and at different cross-stream locations and therefore do not necessarily represent a snapshot of the flow streamlines. However, they do show the basic features of the circulation.

Klymak and Gregg (1999, manuscript submitted to *J. Geophys. Res.*) do a detailed analysis of the circulation during this time. The deep water on the seaward side of the sill is denser than any water on the landward side. On flood tide, this water is lifted over the sill and flows down its landward side as a density current. This is seen in trajectory A. Note that the flow is not along the axis of the inlet, but veers southward following a valley. Shallower water parcels are lifted over the sill and descend the landward side following the density current, but then rebound to reach their level of density. This is seen in trajectory B.

Figure 4 shows an echosounder image taken from the R/V *Miller* on the landward side of the sill along the centerline of the inlet. The arrows indicate the flow measured by the ADCP; water from the seaward side of the sill accelerates into a jet flowing down the land-
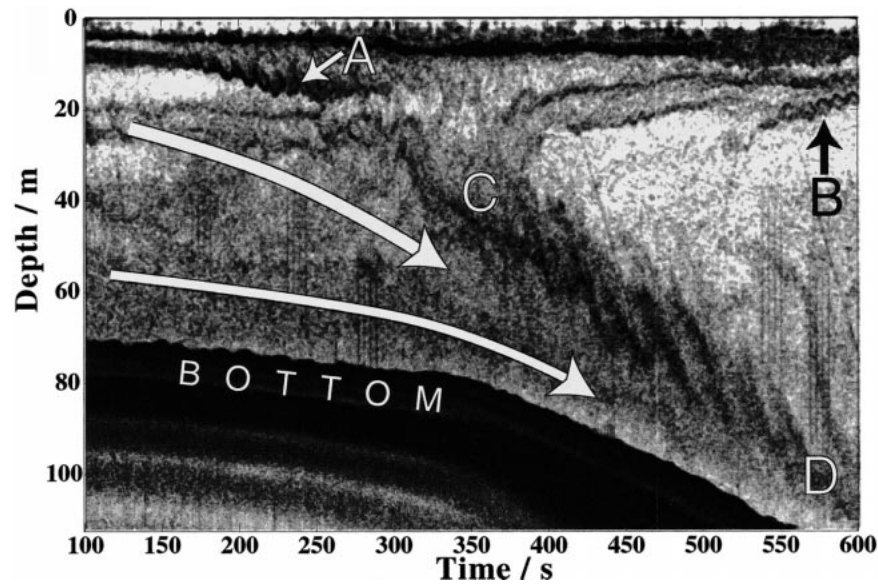
FIG. 4. Echosounder image of flow on the landward side of the Knight Inlet sill during a strong flood on 25 Aug 1995 at approximately 1800 UTC. Three shear layers, marked as "A," "B," and "C" to "D," show Kelvin–Helmholtz billows. The flow of heavy water from the seaward side of the sill is schematically shown by the arrows.

ward side as seen in the float trajectories. Regions of stronger acoustic backscatter are darker. Most of the variations in backscatter intensity, such as the layers in the top 30 m on the left side of the image, are due to variations in the concentrations of plankton. Similar structures are seen everywhere in the inlet. Sometimes turbulent mixing becomes strong enough to create tem-

FIG. 5. Trajectories of all floats that traveled over the sill on strong ebb tides, formatted as in Fig. 3

perature or salinity variations large enough to locally dominate the backscatter (Seim et al. 1995). When the turbulence is due to shear instability, the characteristic Kelvin–Helmholtz billows are seen. Billows are present at the locations marked by "A," "B," and from "C" to "D." The latter marks the upper side of the descending jet. ADCP measurements show this to be the location of a strong shear layer with minimum 2-m shear Richardson numbers well below 0.1. Direct measurements of dissipation rate ε yield peak measured values of about 10^{-4} m^2 s^{-3} in the billows. Heat and mass balances based on cross-channel sections suggest that about 10% of the total flow over sill is mixed through the billow layers (J. Klymak 1998, personal communication). These measurements support our interpretation of the billow layer as a turbulent shear layer.

Figure 5 shows the trajectories of all floats that traveled over the sill during strong ebb tides. Farmer and Armi (1999a) describe the flow in detail. Unlike the flood-tide case, the water coming over sill from the landward side is comparable in density to that at the same level on the seaward side, so a density current is not formed. Instead, the flow either separates from the sill at the downstream edge to form a large shear layer, trajectory A, or forms a hydraulic jump, trajectory B.

Further evidence for strong turbulence is provided by density and microstructure profiles taken near the sill. Regions with unstable density gradients, that is, Thorpe scales, are up to 20 m thick, consistent with the size of the billows in Fig. 4. The Ozmidov scale, $L_O = \varepsilon^{1/2} N^{-3/2}$, which is usually comparable to the rms Thorpe scale, ranges from 2 m to 30 m for the float trajectories for
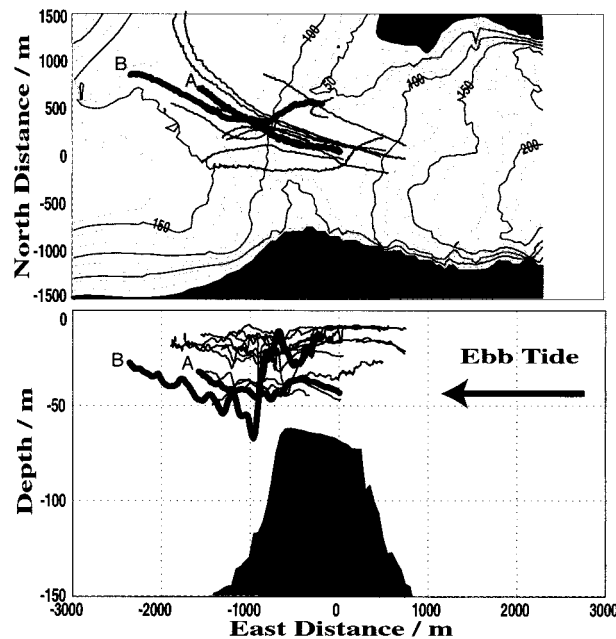
which reliable values of ε and N can be computed (see section 5c). The rms float displacement varies between 1 and 10 times L_0, implying that only a fraction of the vertical motion of the floats could be due to turbulence; some must also be due to waves. Measured values of ε, although probably undersampled, yield averages of order 10^{-5} m^2 s^{-3}. The corresponding diffusivities, $0.2\varepsilon/N^2$, are of order 10^{-2} m^2 s^{-1} (J. Klymak 1998, personal communication).

The flows illustrated in Figs. 3–5 contain both wavelike and turbulent components. The large oscillatory motions in the lee of the sill (Fig. 3) are highly suggestive of internal lee waves. The billows in Fig. 4 are highly suggestive of turbulent shear layers. The overturning and ε measurements show that intense turbulence is present. We will analyze float trajectories from this region and attempt to separate the wave and turbulent components.

5. Observed velocity spectra

a. Spectral estimation

Frequency spectra were computed from segments of the float trajectories chosen to sample different flow regimes. All vertical velocity spectra and most of the horizontal velocity spectra were calculated using multitaper spectral analysis with two tapers (Percival and Walden 1993). Some of the horizontal velocity data contains many gaps due to intermittant acoustic tracking. For these, a Lomb periodogram method is used (Lomb 1976). All spectra are averaged; 95% confidence levels are shown whenever practical.

b. Spectral shapes

Figure 6 shows the depth–time trajectories (a) and frequency spectra (b) of two floats launched together just upstream of the Knight Inlet sill on a strong flood tide. They traverse the sill (14.4–14.8 h), descend its leeward side (14.8–15 h), pass through the shear layer, and enter the turbulent region in the lee of the sill. The same trajectories can be seen in Fig. 3. The data records were each divided into two segments, the first ("On Sill") on top of the sill and the second ("After Sill") in its lee. Each spectrum has a clear break in slope (dashed vertical line). The On Sill segment has the wavelike form shown in Fig. 1b, but, as is typical of these data, there are no nearby CTD profiles to relate the break in slope to N. The After Sill segment is much more energetic and has the turbulent form shown in Fig. 1a. At superbuoyant frequencies it has the -2 spectral slope indicative of an inertial subrange. Again no CTD stations were taken near these data. However, the N profiles in the region landward of the sill are very consistent. Using other profiles from this region yields an N of 0.006–0.2 s^{-1}, which is close to the frequency where the break in slope occurs.
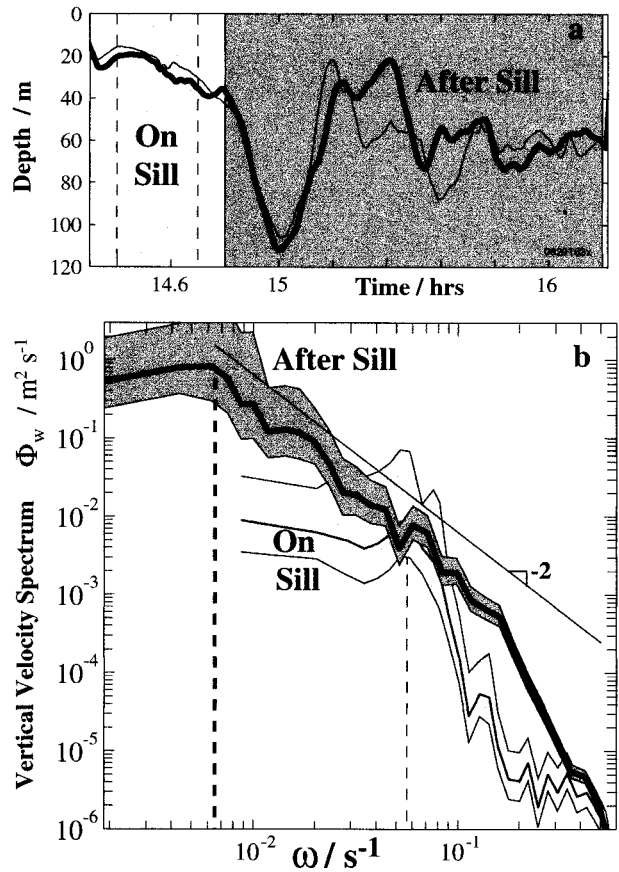

Fig. 6. Spectra from two segments of float trajectories traversing the Knight Inlet sill on a strong flood tide. (a) Trajectories of two floats released simultaneously on the upstream side of the sill. A low-energy region on top of the sill is lightly shaded; a high-energy region in the lee of the sill is darkly shaded. (b) Average frequency spectra from the two floats in the two regions. The dashed lines mark the breaks in slope on each spectrum. The diagonal line has a slope of -2 characteristic of a turbulent inertial subrange. These spectra are not corrected for instrument response.

All 62 vertical velocity spectra, taken together (Fig. 7a), show the same pattern. The data come from Knight Inlet, both near and away from the sill, and from the North Pacific. The categories are mostly self-explanatory. "Knight Inlet Bore" trajectories transit propagating intrusive bores landward of the sill. "Knight Inlet—long deployment" trajectories are from floats deployed overnight, which spent most of their time away from the sill. The spectral levels at low frequencies span a factor of about 3000. Figure 7b shows the same spectra scaled with N as in the Garrett–Munk model. The trends are shown more clearly in Fig. 7c, in which each group of spectra is averaged before plotting.

The spectra show a clear progression from the wavelike form (Fig. 1b) to the turbulent form (Fig. 1a). The most wavelike spectrum ("N. Pacific thermocline") is also the least energetic. The most energetic spectra ("Knight Inlet Flood—across sill") have the turbulent

form. All of these spectra show a break in slope near $\omega = N$. For the wavelike spectra this break is expected since internal waves cannot exist for frequencies greater than N. For the turbulent spectra this is a confirmation of Ozmidov scaling (section 2c) as is discussed in the next section. All of the spectra have subbuoyant energy levels greater than or equal to the GM level. Those with more subbuoyant energy also have more superbuoyant energy and a more turbulent shape. This suggests that there is a progression from wave-dominated dynamics to more turbulent dynamics with increasing energy level. This idea is explored in more detail by D'Asaro and Lien (2000).

c. Ozmidov scaling

Each of the 62 spectra was fit to (4), the universal spectral form for homogeneous turbulence. The model spectrum has two unknown parameters, ω_0 and ε. Both the vertical velocity and the acceleration spectra were fit to their respective model spectra and weighted equally in the fit. The variance of the vertical velocity spectrum is at low frequencies; fitting it provides a good estimate only of ω_0. The variance of the vertical acceleration spectrum is at high frequencies; fitting it provides a good estimate only of ε. Fitting velocity and acceleration simultaneously provides a good estimate of both parameters. The 95% confidence intervals for the estimated values of ε and ω_0 were obtained using a Monte Carlo method. For each spectrum, the estimated values of ε and ω_0 were used to generate a model spectrum using (4). A large number (100) of Gaussian realizations of this model spectrum were generated. Values of ε and ω_0 were estimated for each statistical realization by fitting these realizations as if they were data. The 95% points of the distribution of these ε and ω_0 estimates were computed and used as 95% confidence limits.

Only "turbulent" spectra are fit accurately by (4) since the "wavelike" spectra have a steeper spectral slope for $\omega > \omega_0$. For example, the North Pacific Thermocline spectrum in Fig. 7 is clearly wavelike, while the Knight Inlet Flood—across sill spectra are turbulent. To quantify this, the deviation of each spectrum from the model spectrum was examined using χ^2 tests for all frequencies and for low and high frequencies separately. Both the model spectrum and the observed spectra are flat at low frequencies ($\omega \leq \omega_0$) and show a clear roll off in frequency; accordingly most of the observed spectra pass the χ^2 test at low frequencies and yield accurate estimates of the roll-off frequency ω_0. The model spectrum and the wavelike spectra differ for $\omega > \omega_0$. Thus only the 25 spectra that pass the χ^2 test at high frequencies will yield accurate estimates of ε.

Figure 8 compares ω_0 and N for all spectra. The mean value of N/ω_0 is 2 ± 0.3. The results do not change much if only spectra that pass the χ^2 test at high frequencies are used. Individual estimates of N have a large

uncertainty [see section 3c(2)]; the vertical error bars, showing the range in N over the depth of each trajectory, reflect this. Average 95% confidence limits for an individual N are 0.7 ω_0 and 6.4 ω_0.

Despite the uncertainties, ω_0 is closely related to N. For the "turbulent" spectra, this is a direct confirmation of Ozmidov scaling: The largest turbulent eddies of the inertial subrange have an average frequency of approximately N.

d. Waves versus turbulence

1) WAVE SPECTRA

Figure 9 shows the horizontal and vertical velocity spectra from a single float deployed in the North Pacific thermocline (see DFOD Fig. 5 for more analysis of these data). The spectra lie very close to the Garrett–Munk spectrum (orange dashed line) for frequencies below N. The vertical velocity spectrum falls rapidly above N. The black line marked W_{iw} shows the vertical velocity spectrum computed from (2) assuming that the horizontal velocity spectrum is entirely due to internal waves. If (2) is true, W_{iw} should equal W. Here W_{iw} lies within the error bars for W up to about 0.4N. We conclude that internal waves dominate these data, as expected.

Figure 10 shows the horizontal and vertical velocity spectra from three float-trajectory segments from Knight Inlet. These were chosen to have low energy and to show a break in slope at the same frequency so that they could be averaged. All are many hours in duration and do not cross the sill. The spectral levels are only slightly above the GM spectrum (orange dashed line), and the horizontal and vertical spectra are consistent with (2) except very near N. The east (red, U) velocity spectrum is more energetic than the north (green, V) velocity spectrum, reflecting the east–west alignment of the inlet. The vertical velocity spectrum increases slightly with frequency. These spectra taken a few kilometers from the very energetic Knight Inlet sill are nearly indistinguishable from the open ocean spectra in Fig. 9. This is remarkable.

Plots similar to Figs. 9 and 10, but using Eulerian data, are the major historical justification for believing that the oceanic velocity and density fluctuations with frequencies between N and f are due to internal waves (Fofonoff 1969; Müller and Siedler 1976; Müller et al. 1978). Such analyses usually fail close to N, as does Fig. 9. Desaubies (1975) argues that this represents a failure of the WKB approximation when N varies with depth and not a failure of internal wave physics.

2) WAVE AND TURBULENCE SPECTRA

(i) Selection

The region near the Knight Inlet sill contains a mixture of waves and turbulence (see section 4). A total of
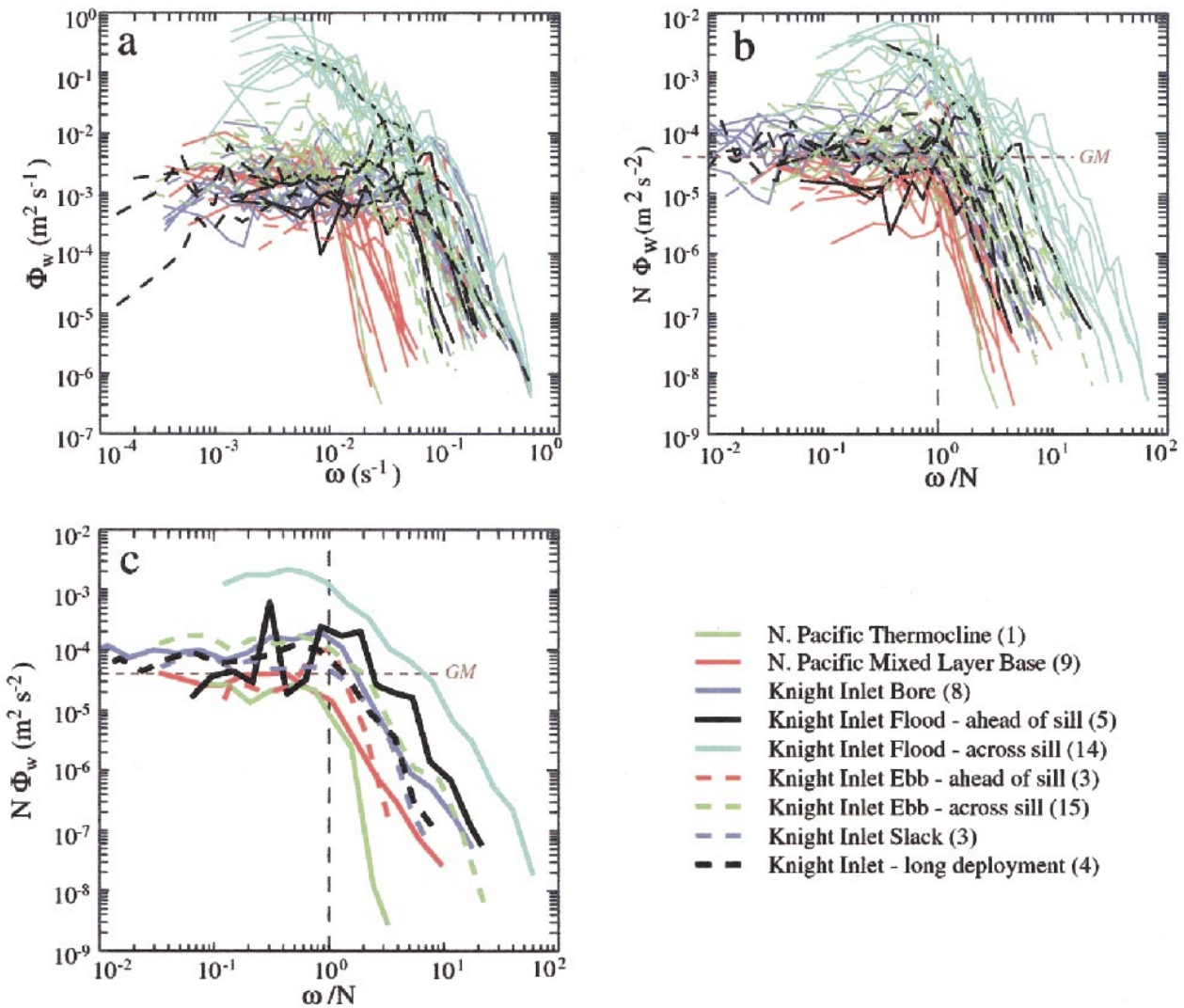
FIG. 7. Spectra of vertical velocity from Knight Inlet and the North Pacific. Color indicates subgroup of spectra as shown on lower right. No corrections for instrument response have been made. Number in legend indicates number of spectra in each subgroup. (a) Raw spectra, (b) spectra scaled by N as in GM model, (c) N-scaled spectra averaged in each subgroup. The GM spectral energy level is shown in (b) and (c).

29 trajectories is available from this region; one is too noisy to use. "High accuracy" acoustic tracking is available for 9 of the remaining 28 spectra; the horizontal velocity spectra for these are accurate to about $10N$; horizontal velocity spectra for the "low accuracy" trajectories are not accurate past $2N$. Figure 11 shows all 28 spectra. Most (78%) of the vertical velocity spectra fits Eq. (4), shown by the orange line labeled W_{turb}, at the 95% level. All fit (4) at superbuoyant frequencies. The blue dots show these spectra, corrected for instrument response following (6). Their average (blue line) fits (4) remarkably well.

(ii) Scaling

The vertical velocity spectra are scaled so that those fitting (4) would collapse to a single curve; ε and ω_0

are estimated for each spectrum as described in section 5c. The value of N is estimated as $2\omega_0$ since this is more reliable and consistent than using the CTD-derived values (see section 5c and Fig. 8). The horizontal velocity spectra are scaled in the same way as the vertical velocity spectra. Note that the horizontal and vertical velocity spectra are computed from completely different data, acoustic tracking and float pressure, respectively.

(iii) Consistency tests

Figure 11 shows the scaled horizontal and vertical velocity spectra. Here W_{iw} lies within the error bars for W up to about $0.3N$, implying that (2) applies to these data. Near N, the observed motions become isotropic, whereas (2) predicts more vertical kinetic energy than horizontal kinetic energy.
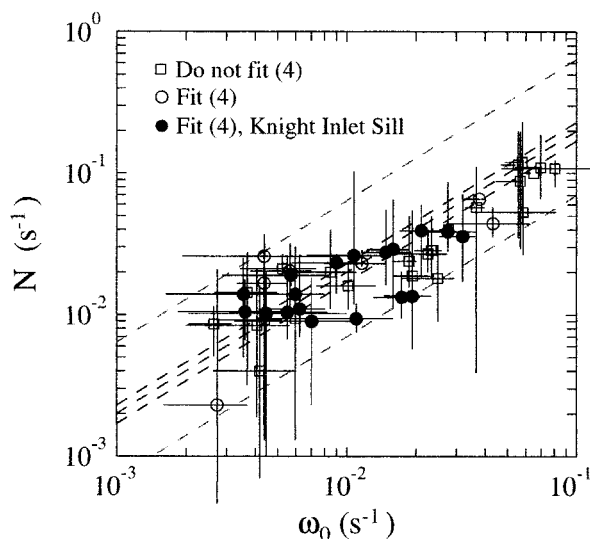
FIG. 8. Comparison between the buoyancy frequency N and the "large-eddy" frequency ω_0 for the spectra in Fig. 7; ω_0 is obtained by fitting (4) to the spectrum as described in the text. Spectra that are accurately fit by (4) are shown by circles; those that do not are shown by squares. Filled circles are from the Knight Inlet sill. Vertical lines are 95% ranges of N over the depth range of the float trajectory obtained from nearby CTD profiles; horizontal lines are the 95% confidence limits for ω_0. The mean ratio between N and ω_0 is 2 ± 0.3, shown by the three central dashed lines; the average 95% confidence level on individual values of N is shown by the outer dashed lines.

FIG. 10. Normalized east (red), north (green), and vertical (blue) velocity spectra from quiet regions of Knight Inlet. Shading represents the 95% confidence interval. Black line (W_{iw}) is the vertical velocity spectrum computed from (2). Orange dashed lines are the GM spectrum.
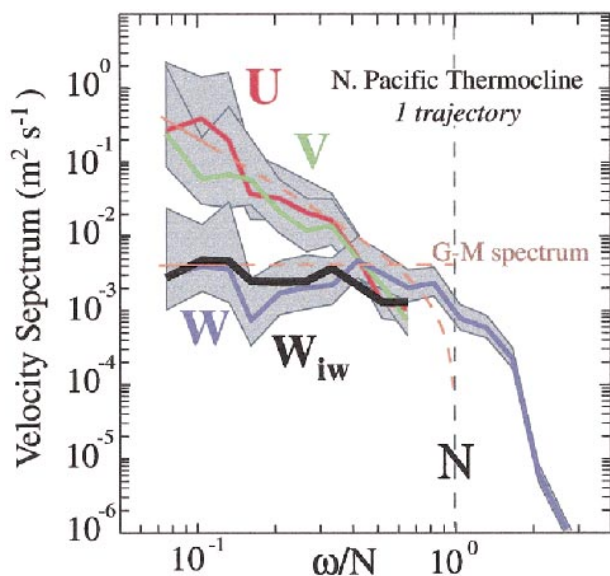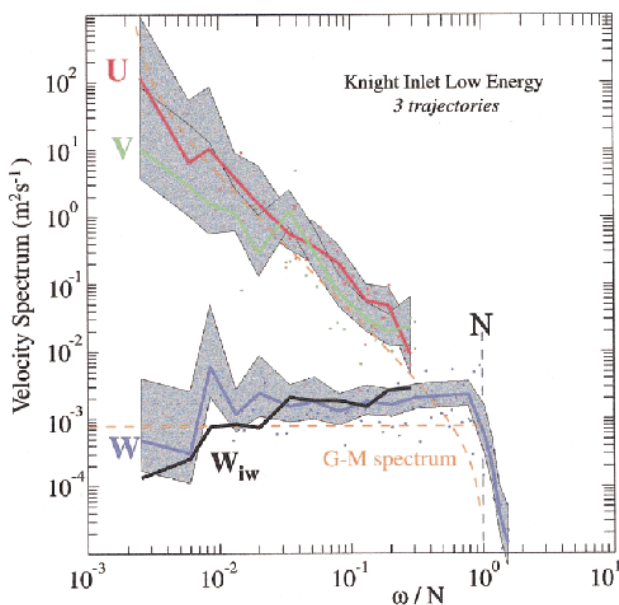

FIG. 9. Normalized east (red), north (green), and vertical (blue) velocity spectra from the North Pacific thermocline. Shading represents the 95% confidence interval. Black line (W_{iw}) is the vertical velocity spectrum computed from (2). Orange dashed lines are the GM spectrum.
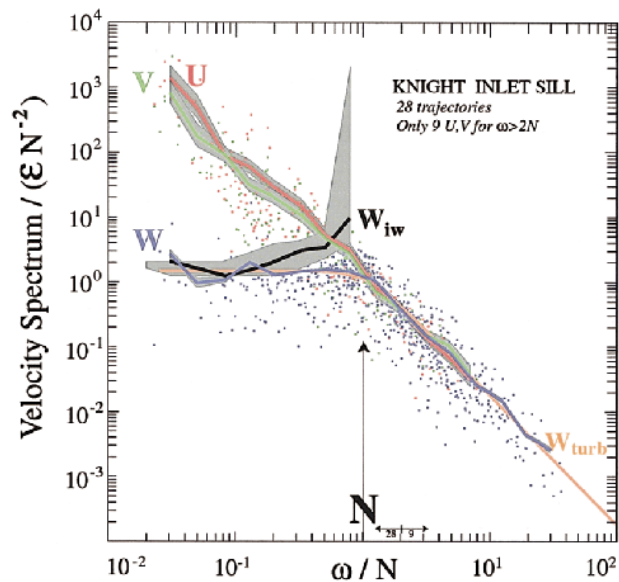

FIG. 11. Normalized east (red), north (green), and vertical (blue) velocity spectra from the Knight Inlet sill. Of these, 22 fit Eq. (4), the orange line, and 9 have high accuracy tracking. Dots are individual spectral estimates corrected for instrumental response; lines are average of these; shading represents the 95% confidence interval. Black line (W_{iw}) is the vertical velocity spectrum computed from (2) assuming that horizontal spectra are entirely due to internal waves. A major source of error in W_{iw} results from the uncertainty in N. The solid black line uses the best guess, $N = 2\omega_0$, from Fig. 8; the surrounding shaded region shows the total error in W_{iw} including that due to a variation in N of 0.7–6.4 ω_0.

The subbuoyant motions have the properties expected of internal waves: they are anisotropic, approximately as specified by (2), and have approximately the GM spectral shape characteristic of internal waves. The superbuoyant motions have the properties expected of homogeneous turbulence: their spectra are isotropic, and they have the spectral shape characteristic of homogeneous turbulence. A range of frequencies near N appears to be transitional between these two types of motions. This is the main result of the paper.

(iv) Rationalization

Internal waves are clearly only subbuoyant. A simple scaling argument can help explain why turbulence is only superbuoyant. Consider a turbulent flow with typical velocity U and particle displacement $X = U/\omega$. The typical spatial scale is also X. The terms in the momentum equation scale as

$$\frac{Du}{Dt} \qquad u \cdot \nabla u \qquad \frac{g}{\rho_0}\rho \qquad \frac{1}{\rho_0}\nabla P$$
$$\omega U \qquad UU/X \qquad N^2 X$$
$$\omega^2 X \qquad \omega^2 X \qquad N^2 X. \qquad (8)$$

Turbulence requires that the inertial forces be larger than the buoyancy forces. The scaling shows that this can occur only for superbuoyant frequencies.

6. Parameterization

The 28 spectra in Fig. 11 have a nearly universal form that spans the boundary between waves and turbulence. This spectral form implies a parameterization for the turbulence in terms of the waves (and vice versa).

We assume a vertical velocity spectrum of form (3), $\Phi_w = \beta\varepsilon\omega^{-2}B(\omega/\omega_0)$, with B given by (5). Although this spectrum was derived for homogeneous turbulence, it fits the Knight Inlet sill data well. We use Ozmidov scaling (section 5c) and assume $N = 2\omega_0$. For $\omega \ll N$, Φ_w is white and has a level $\Phi_w^{\text{wave}} = 1.5\varepsilon N^{-2}$. Integrating Φ_w yields the total vertical velocity variance $q_w^2 = 3\varepsilon/N$. Combining these expressions and using $\beta = 1.8$ yields

$$\varepsilon = 1.2\beta^{-1}\Phi_w^{\text{wave}}N^2 = 0.6\beta^{-1}q_w^2 N. \qquad (9)$$

Similarly, the turbulent diffusivity, computed from the Osborn (1980) formula, is

$$K_\rho = \gamma\varepsilon N^{-2} = 1.2\gamma\beta^{-1}\Phi_w^{\text{wave}}, \qquad (10)$$

where γ is about 0.2 for wave-driven turbulence (Imberger and Ivey 1991). The diffusivity can therefore be read directly off the vertical axis in Fig. 7 for those spectra that match the universal shape. For Knight Inlet, K_ρ estimated in this way varies from 0.001 m^2 s^{-1} to about 0.1 m^2 s^{-1}, comparable to the range estimated from microstructure profiles (J. Klymak 1998, personal communication).

Clearly, this parameterization is not always valid. It certainly does not apply when the velocity spectra are of the Garrett–Munk form. For these relatively low energy environments the forms proposed by Gregg (1989) and Polzin et al. (1995) apply. It should apply in higher energy environments, such as Knight Inlet. D'Asaro and Lien (2000) discuss this in more detail and argue that (9) and (10) apply in a ''stratified turbulence'' regime with sufficiently high energy that wave–wave interactions can be neglected.

For the observed Lagrangian spectra, the horizontal kinetic energy is mostly subbuoyant. The ratio of subbuoyant to superbuoyant horizontal kinetic energy is not universal but is set by the low-frequency cutoff of the internal wave spectrum. It should therefore depend on external parameters such as the size of the domain or the inertial frequency. If the low-frequency cutoff is much less than N, then the horizontal kinetic energy will be mostly due to waves. In contrast, the vertical kinetic energy is split equally between subbuoyant and superbuoyant frequencies; three-quarters of the energy has a frequency greater than $N/2$. Thus the horizontal kinetic energy is mostly waves, whereas the vertical kinetic energy is approximately half turbulence.

Turbulence parameterization models often try to relate energy dissipation ε to kinetic energy q^2. In a stratified fluid with a strong wave component, kinetic energy becomes highly anisotropic, with the wave energy concentrated in the horizontal component. Traditional relationships for turbulence, such as $\varepsilon = q^2/T_t$, are unlikely to work well when using the horizontal or total kinetic energies because these are dominated by wave energy. They are more likely to work when using the vertical kinetic energy, as in Eq. (9), since this still has a large turbulent component. This is consistent with recent results by Briggs et al. (1998).

7. Summary and discussion

a. Results

A set of 52 Lagrangian float trajectories from Knight Inlet and 10 trajectories from below the mixed layer in the wintertime northeast Pacific were analyzed using frequency spectra. The strongest turbulence occurred near the Knight Inlet sill, where a complex mix of internal waves and turbulence coexisted. Key results are as follows:

- Vertical velocity spectra from the float trajectories show a progression from a nearly Garrett–Munk internal wave spectrum at low energies to a shape characteristic of homogeneous turbulence at high energies (Fig. 7).
- All spectra show a break in slope at a frequency close to the buoyancy frequency N (Figs. 7 and 8).
- Vertical velocity spectra from all of the trajectories that crossed the Knight Inlet sill fit the universal form for homogeneous turbulence (Lien et al. 1998) for frequencies greater than N (Fig. 11).

- The ratio of the horizontal to vertical velocity for all spectra obeys the internal wave consistency relation (2) for Lagrangian frequencies much less than N. For the Knight Inlet sill spectra, the ratio is 1 for frequencies greater than N. It cannot be determined for other spectra.
- All spectra have more horizonal than vertical kinetic energy. This anisotropy is almost entirely due to motions with Lagrangian frequencies less than N.

b. Discussion

The classification of a given flow as ''waves'' or ''turbulence'' is always problematic (and thus controversial) since neither term can be defined exactly. Some flows are certainly more turbulent or wavelike than others, as discussed in the introduction. Our analysis suggests that Lagrangian frequency separates waves from turbulence. This is a bold statement and needs to be considered carefully.

We classify superbuoyant motions as turbulence because they are nearly isotropic and exhibit the same inertial subrange found in unstratified turbulent flows. These motions have a kinetic energy of $Q_t^2 \approx \beta \varepsilon / N$, the triangular area to the right of N in Fig. 11. Their time scale $T_t = Q_t^2 / \varepsilon$ is, of course, approximately N^{-1}. Their length scale $L_t = Q_t T_t \approx (\varepsilon / N^3)^{1/2}$ equals the Ozmidov scale, L_O. Our result is thus equivalent to stating that the largest turbulent eddies in a stratified fluid have a size of about L_O. This has been well documented in studies of the ocean thermocline (Dillon 1982; Moum 1996) and in laboratory studies of stratified flows (Itsweire et al. 1986; De Silva and Fernando 1992) and stratified shear flows (Rohr et al. 1988) and should not be surprising.

We classify subbuoyant motions as internal waves because they are consistent with Eq. (2) and have a nearly GM spectral form. We do not claim, however, that these motions can be accurately described by the equations for linear internal waves in an ocean otherwise at rest. Flow near the Knight Inlet sill is critically controlled (Farmer and Armi 1999a), so the velocities are comparable to the internal wave phase speeds. This flow cannot be described by internal waves in an ocean otherwise at rest. Similar arguments can be made for the smaller scales of the open-ocean internal wave field (Müller et al. 1986). Henyey et al. (1986) successfully predict energy transfer through an internal wave field by modeling the propagation of individual ''test waves'' through the background flow produced by larger waves. These test waves are not linear in a coordinate system at rest with the earth, but they are locally linear in a Lagrangian frame. Each wave, and the sum of all waves, obeys (2), where ω is the Lagrangian frequency. Our data are consistent with this view of internal wave dynamics. That this applies in the highly complex and nonlinear flow of Knight Inlet is surprising.

These considerations do not exclude the possibility of some subbuoyant motions that are not internal waves. The W_{iw} spectrum lies above the W spectrum in Fig. 11 for nearly a decade of frequencies below N. This could be due either to non-WKB effects of internal waves or to noninternal wave motions with much more horizontal than vertical kinetic energy. Open ocean measurements show a similar excess of horizontal kinetic energy. Müller et al. (1986), Lien and Müller (1992), and D'Asaro and Morehead (1991) interpret this as due to a ''vortical mode'' consisting of nearly two-dimensional, horizontal turbulence. If such motions exist in our data, they are too weak to detect or are confined to a small frequency band near N or to low frequencies, which do not enter our analysis.

The division between waves and turbulence is not sharp. Motions with frequencies near N are presumably transitional between waves and turbulence, perhaps representing the instabilities that convert wave energy to turbulence. Our results suggest that such nonlinear ''breaking'' internal waves and other ''large eddy'' structures of the turbulence have dominant frequencies near N.

Observed vertical velocity spectra sometimes show a peak near N. Our parameterization, which relies on matching smooth spectra at N, is more difficult to justify when this peak is present. If the peak results from nearly linear, low mode waves superimposed on an underlying smooth spectrum, then the peak presents no fundamental problem. This, however, is not assured.

These measurements were taken in a regime with both strong stratification and strong mean shear, $\mathbf{S} = \partial \mathbf{U} / \partial z$. Thus it is possible that the shear timescale, S^{-1}, rather than the buoyancy timescale, could control the turbulence (Fernando and Hunt 1996; Schumann and Gertz 1995). We do not have accurate shear measurements along the float trajectories. On average, N and S, measured on the scale of a few meters, have a similar magnitude in Knight Inlet. Thus we cannot tell which is more important.

Most of our data are from a particular, and perhaps peculiar, location for a limited period of time. If, however, our results are more generally true, they have a significant impact on our understanding of mixing in stratified fluids. If Lagrangian frequency does indeed separate waves from turbulence, useful models of stratified turbulence could perhaps be constructed with separate submodels for the subbuoyant, anisotropic wavelike component and the superbuoyant, isotropic turbulent component. Expressions like (9) would link the two components. Since stratified fluids can support waves, models that explicitly recognize this are likely to be an improvement over models that do not.

Many questions remain. The most urgent issues are the dependence of our results on spatial scale and the addition of shear and Richardson number to the data. Does the split between waves and turbulence occur at both large and small scales? Does the Richardson number confirm the transition from waves to turbulence at

N by passing through a critical value? Do measurements of fluxes confirm this? Presumably the turbulence and its fluxes are concentrated near time and space scales defined by N and L_O, where the Richardson number is small. Internal waves and their fluxes occur at larger scales and lower frequencies and are thus subject to a smaller Richardson number. We touch on some of these issues in D'Asaro and Lien (2000), but they are unlikely to be settled without further measurements or simulations.

REFERENCES

Briggs, D. A., J. H. Ferziger, J. R. Koseff, and S. G. Monismith, 1998: Turbulent mixing in a shear-free stably stratified two-layer fluid. *J. Fluid Mech.,* **354,** 175–208.

Corrsin, S., 1957: On the spectrum of isotropic temperature fluctuations in an isotropic turbulence. *J. Appl. Phys.,* **22,** 469–473.

D'Asaro, E. A., and M. D. Morehead, 1991: Internal waves and velocity fine structure in the Arctic Ocean. *J. Geophys. Res.,* **96** (C7), 12 725–12 738.

——, and G. T. Dairiki, 1997: Turbulence intensity measurements in a wind driven mixed layer. *J. Phys. Oceanogr.,* **27,** 2009–2022.

——, and R. C. Lien, 2000: The wave–turbulence transition in stratified flows. *J. Phys. Oceanogr.,* in press.

——, D. M. Farmer, J. T. Osse, and G. T. Dairiki, 1996: A Lagrangian float. *J. Atmos. Oceanic Technol.,* **13,** 1230–1246.

Desaubies, Y. J. F., 1975: A linear theory of internal wave spectra and coherences near the Väisälä frequency. *J. Geophys. Res.,* **80** (6), 895–899.

De Silva, I. P. D., and H. J. S. Fernando, 1992: Some aspects of mixing in a stratified turbulent patch. *J. Fluid Mech.,* **240,** 601–625.

Dillon, T. M., 1982: Vertical overturns: A comparison of Thorpe and Ozmidov length scales. *J. Geophys. Res.,* **87,** 9601–9613.

Farmer, D. M., and J. D. Smith, 1980: Tidal interaction of stratified flow with a sill in Knight Inlet. *Deep-Sea Res.,* **27A,** 239–254.

——, and H. J. Freeland, 1983: The physical oceanography of fjords. *Progress in Oceanography,* Vol. 12, Pergamon, 147–220.

——, and L. Armi, 1999a: The generation and trapping of internal solitary waves over topography. *Science,* **283,** 188–190.

——, and ——, 1999b: Stratified flow over topography: The role of small scale entrainment and mixing in flow establishment. *Proc. Roy. Soc. London,* **A455,** 3221–3258.

Fernando, H. J. S., and J. C. R. Hunt, 1996: Some aspects of turbulence and mixing in stably stratified layers. *Dyn. Atmos. Oceans,* **23,** 35–62.

Fofonoff, N. P., 1969: Spectral characteristics of internal waves in the ocean. *Deep-Sea Res.,* **16S,** 59–71.

Fung, J. C. H., J. C. R. Hunt, N. A. Malik, and R. J. Perkins, 1992: Kinematic simulation of homogeneous turbulence by unsteady random Fourier modes. *J. Fluid Mech.,* **236,** 281–318.

Gargett, A. E., T. R. Osborn, and P. W. Nasmyth, 1984: Local isotropy and the decay of turbulence in a stratified fluid. *J. Fluid Mech.,* **144,** 231–280.

Garrett, C. J. R., and W. H. Munk, 1975: Space–time scales of internal waves: A progress report. *J. Geophys. Res.,* **80,** 291–297.

Gertz, T., and H. Yamazaki, 1993: Direct numerical simulation of buoyancy-driven turbulence in a stably stratified fluid. *J. Fluid Mech.,* **249,** 415–440.

Gregg, M. C., 1989: Scaling turbulent dissipation in the thermocline. *J. Geophys. Res.,* **94,** 9686–9698.

Hanazaki, H., and J. C. R. Hunt, 1996: Linear processes in unsteady stably stratified turbulence. *J. Fluid Mech.,* **318,** 303–337.

Henyey, F. S., J. Wright, and S. M. Flatté, 1986: Energy and action flow through the internal wave field: An eikonal approach. *J. Geophys. Res.,* **91,** 8487–8495.

Holt, S. E., J. R. Koseff, and J. H. Ferziger, 1992: A numerical study of the evolution and structure of homogeneous stably stratified sheared turbulence. *J. Fluid Mech.,* **237,** 499–539.

Imberger, J., and G. N. Ivey, 1991: On the nature of turbulence in a stratified fluid. Part I: The energetics of mixing. *J. Phys. Oceanogr.,* **21,** 650–658.

Itsweire, E. C., K. N. Helland, and C. W. VanAtta, 1986: The evolution of grid-generated turbulence in a stably stratified fluid. *J. Fluid Mech.,* **162,** 299–338.

Lien, R. C., and P. Müller, 1992: Normal mode decomposition of small scale oceanic motions. *J. Phys. Oceanogr.,* **22,** 1583–1595.

——, E. A. D'Asaro, and G. T. Dairiki, 1998: Lagrangian frequency spectra of vertical velocity and vorticity in high-Reynolds number oceanic turbulence. *J. Fluid Mech.,* **362,** 177–198.

Lin, C. L., J. H. Ferziger, J. R. Koseff, and S. G. Monismith, 1995: Simulation and stability of two-dimensional internal gravity waves in a stratified shear flow. *Dyn. Atmos. Oceans,* **19,** 325–366.

Lomb, N., 1976: Least-squares frequency analysis of unequally spaced data. *Astrophys. Space Sci.,* **39,** 447–462.

Moum, J. N., 1996: Energy-containing scales of turbulence in the ocean thermocline. *J. Geophys. Res.,* **101** (C6), 14 095–14 110.

Müller, P., and G. Siedler, 1976: Consistency relations for internal waves. *Deep-Sea Res.,* **23,** 613–628.

——, D. J. Olbers, and J. Willebrand, 1978: The IWEX spectrum. *J. Geophys. Res.,* **83,** 479–500.

——, G. Holloway, F. Henyey, and N. Pomphrey, 1986: Nonlinear interactions among internal gravity waves. *Rev. Geophys,* **24,** 493–536.

Osborn, T. R., 1980: Estimates of the local rate of vertical diffusion from dissipation measurements. *J. Phys. Oceanogr.,* **10,** 83–89.

Ozmidov, R. V., 1965: On the turbulent exchange in a stably stratified ocean. *Izv. Acad. Sci. USSR, Atmos. Oceanic Phys.,* **1,** 853–860.

Percival, D. B., and A. T. Walden, 1993: *Spectral Analysis for Physical Applications.* Cambridge University Press, 583 pp.

Phillips, O. M., 1977: *The Dynamics of the Upper Ocean.* 2d ed. Cambridge University Press, 344 pp.

Polzin, K., J. Toole, and R. Schmitt, 1995: Finescale parameterizations of turbulent dissipation. *J. Phys. Oceanogr.,* **25,** 306–328.

Rohr, J. J., E. C. Itsweire, K. N. Helland, and C. VanAtta, 1988: Growth and decay of turbulence in a stably stratified shear flow. *J. Fluid Mech.,* **195,** 77–111.

Schumann, U., and T. Gertz, 1995: Turbulent mixing in stably stratified flows. *J. Appl. Meteor.,* **34,** 33–48.

Seim, H. E., M. C. Gregg, and R. T. Miyamoto, 1995: Acoustic backscatter from turbulent microstructure. *J. Atmos. Oceanic Technol.,* **12,** 367–380.

Stacey, M. W., and S. P. Pond, 1997: On the Mellor–Yamada turbulence closure scheme: The surface boundary condition for q^2. *J. Phys. Oceanogr.,* **27,** 2081–2086.

Stewart, R., 1969: Turbulence and waves in a stratified atmosphere. *Radio Sci.,* **4,** 1269–1278.

Stillinger, D. C., K. N. Helland, and C. W. VanAtta, 1983: Experi-ments on the transition of homogeneous turbulence to internal waves in a stratified fluid. *J. Fluid Mech.,* **131,** 91–122.

Winters, K. E., and E. A. D'Asaro, 1994: Three-dimensional wave instability near a critical level. *J. Fluid Mech.,* **272,** 255–284.

——, and ——, 1997: Direct simulation of internal wave energy transfer. *J. Phys. Oceanogr.,* **27,** 1937–1945.